Journal of Power Sources 453 (2020) 227849

Contents lists available at ScienceDirect

Journal of Power Sources

journal homepage: www.elsevier.com/locate/jpowsour

Transient modeling and simulation of a nonisothermal sodium–sulfur cell

Sarah Schaefer (Caprio), Sai Pushpitha Vudata, Debangsu Bhattacharyya *, Richard Turton

Department of Chemical and Biomedical Engineering, West Virginia University, Morgantown, WV, 26506, USA

HIGHLIGHTS

- First-principles, thermal-electrochemical dynamic model of the Na–S cell presented.
- Model validated using experimental data under varying current density operation.
- Higher cell temperature observed during discharge compared to charge.
- Higher current density operation leads to higher cell temperature.
- Higher temperature operation can improve cell efficiency.

ARTICLE INFO

Keywords:
Sodium sulfur battery
beta"-alumina transient model
Nonisothermal
Peltier heat
Physicochemical

ABSTRACT

The use of sodium-sulfur batteries at the grid level requires high current density operation that can cause cell deterioration, leading to lower sulfur utilization and lower energy efficiency. In addition, it can result in undesired thermal runaway leading to potentially hazardous situations. A rigorous, dynamic model of a sodium-sulfur battery can be used to study these phenomena, design the battery for optimal transient performance, and develop mitigation strategies. With this motivation, a first-principles, fully coupled thermal-electrochemical dynamic model of the entire sodium-sulfur cell has been developed. The thermal model considers heat generation due to Ohmic loss, Peltier heat, and heat due to entropy change. Species conservation equations are written in the sulfur electrode by considering the phase transition and change in the composition depending on the SOD. Species conservation equations are written in the beta"-alumina electrolyte for the ionic species by considering the change in composition due to diffusion and migration. In addition, the potential distribution, and cell resistance for this spatially distributed system has been modeled. Furthermore, temperature-dependent correlations for the physicochemical properties are developed. The model is used to study both charging and discharging characteristics of the cell at varying current densities.

1. Introduction

Renewable energy sources such as wind and solar have been growing at a remarkable rate over the last several years. However, these energy sources are intermittent and vary irrespective of the demand [1]. Therefore, fossil-fueled power sources are playing a critical role by rapidly changing their load to take care of the imbalance between the demand and supply. However, rapid load-following and low-load operation causes efficiency loss and have adverse effects on the plant health [2,3]. Energy storage, especially at large-scale, can reduce the imbalance to a great extent thus addressing some of the major issues caused by the increasing integration of renewables into the grid [4–7].

Energy can be stored on a large scale in various storage systems like pumped hydroelectric, compressed air energy storage (CAES), battery energy storage systems (BESS), etc. However, pumped hydroelectric and CAES are large energy storage systems and require certain geographical formations that are often located far from the locations where electricity is needed. BESS are modular and do not need any geographical formations [8–10]. Moreover, smaller systems have typically faster ramp rates compared to larger units [11]. BESS are highly scalable and have fast response time to peak shaving and load shifting, improving the grid reliability and stability [8,12]. Further, BESS are suitable for on/off operations and can be centrally located or distributed [13].

Depending on the combinations of materials and chemicals used, a wide range of battery technologies is available [7–10]. For grid-level storage, various secondary battery technologies are of main interest since they can be discharged and charged repeatedly, have high energy densities, low self-discharge rates, and long life-times. Rechargeable

* Corresponding author. West Virginia University, Department of Chemical and Biomedical Engineering, Morgantown, WV, 26506, USA.
E-mail address: Debangsu.Bhattacharyya@mail.wvu.edu (D. Bhattacharyya).

https://doi.org/10.1016/j.jpowsour.2020.227849
Received 23 August 2019; Received in revised form 19 January 2020; Accepted 4 February 2020
0378-7753/© 2020 Elsevier B.V. All rights reserved.

Li-ion batteries are currently being widely evaluated as a promising technology since they have significantly high energy density and a long cycle life [14,15]. However, Coulombic overheating and high costs are the major constraints for large-scale commercialization of Li-ion technology. Therefore, the ongoing need to store energy more safely, compactly and affordably motivates continued research on alternative battery technologies [16–19]. Sodium is the second lightest alkali metal. Using sodium in the anode coupled with an appropriate cathode material can help to achieve high specific energy density and high open circuit voltage at a lower cost compared to Li-ion batteries [19–22].

When liquid sulfur is used in the cathode with beta"-alumina as the electrolyte, the resulting sodium sulfur (NaS) battery yields high energy density, low cost of the reactants, high open-circuit voltage and comparatively inexpensive cathode and anode making the NaS battery an ideal candidate for grid-level energy storage applications [23,24]. The NaS batteries can be operated under room temperature [25–27] but room-temperature NaS batteries have a low capacity retention and poor cycling properties [18]. For grid-level storage applications, high-temperature sodium-sulfur batteries are of main interest. These batteries typically operate at 300–400 °C and have the desired favorable characteristics as discussed earlier for grid-level storage applications. However, one of the issues of these batteries is thermal runaway especially under high energy-density operation. For developing an efficient thermal management system, a detailed dynamic model of the entire cell that can capture the nonlinearities of the NaS cells under changing operating conditions will be critical.

There is a lack of research literature on modeling of sodium-sulfur cells/batteries in the public domain. Sudworth and Tilley [22] described the development of sodium-sulfur batteries, principles of their operation, design and manufacture, performance and safety as well as prototype demonstrations. β″- alumina electrolyte shows high sodium ion conductivity at high temperature, which helps the Na–S battery to operate effectively at low loss. Initially the cell remains in the two phase region containing mainly sulfur along with some amount of sodium polysulfide depending on the SOD. As reactions proceed, the sulfur electrode becomes single phase containing only polysulfide. As a result, not only does the capacity get reduced, but also the cell voltage (EMF) gets affected. The cell voltage and capacity depend on the potential profile and electrochemical reaction rates in the electrodes as well as the sodium ion conductivity of the electrode – all of which are strongly affected by the operating temperature of the cell [28–32]. The SOD also affects the cell resistance and the heat generation rate and entropy [33,34]. However, the cell potential profile as well as other key variables are also affected due to the inhomogeneous composition of the sulfur electrode. Kawamoto [35] investigated the 2-D distribution of the melt in sulfur electrode and observed that at high current density, the non-uniformity in the melt increases thus decreasing the sulfur utilization. For grid-connected application, high energy density operation of the batteries is of significant interest. However, high energy density operation causes low sulfur utilization, low energy efficiency and unusual temperature rise due to high heat generation rates. Kawamoto and Kusakabe [36] have investigated the high current density operation of a single sodium sulfur cell, but the impact of concentration polarization was neglected. Kawamoto [37] developed a non-isothermal dynamic model by capturing the spatial variation of the cell voltage and ion concentration profile, but only the sulfur electrode was modeled. The effect of temperature and mole fraction of electrolyte on the sodium ion diffusion coefficient in the sulfur electrode was also neglected.

Existing literature that has focused on modeling the NaS batteries, uses considerably simpler models of the cell. Hussein and Cheung [38] developed an equivalent circuit model for a NaS battery where, the heat transfer characteristics of individual cells were not considered. For small power systems, Sarasua and Molina [39] developed a simple battery model to analyze the thermal behavior of NaS battery. Min and Lee [40] developed a steady state lumped thermal model for an entire cell, as well as a battery module. Aygun [41] incorporated a two dimensional heat transfer model with an electrochemical model, which can be used as a computational design tool to calculate the two dimensional distribution of temperature inside a NaS battery. Most of the papers cited above neglected the variation of thermo-physical properties with temperature. However, dynamic characteristics of the cell/battery are affected considerably by the varying thermo-physical properties with temperature. Therefore, correlations were developed in this paper to understand the cell performance under different ambient conditions.

Overall, there is a lack of studies in the open literature on detailed, non-isothermal dynamic model of the entire sodium sulfur cell by considering both the electrochemical as well as thermal phenomena using temperature-dependent correlations for thermophysical properties. Such models are very useful for studying the high current-density operations and large ramp rates as would be expected in grid-connected operations. As noted above, the operation of sodium sulfur cells at high current density with large ramp rates can cause cell performance loss due to lower sulfur utilization and lower energy efficiency. In addition, these demanding operations can result in undesired thermal runaway leading to potentially hazardous situations. The model developed in this work is validated with the experimental data from the literature. The validated model is used to study the cell dynamics under various load-following conditions.

2. Model development

The battery considered in this study consists of a central molten sodium electrode, beta"-alumina solid ceramic electrolyte, and an outer molten sulfur/sodium-polysulfide electrode as shown in Fig. 1.

The half-cell reactions that take place in the sodium and sulfur electrodes, respectively, are given by:

$$2Na \leftrightarrow 2Na^{+} + 2e^{-} \tag{1}$$

$$2Na^{+} + xS + 2e^{-} \leftrightarrow Na_2S_x \tag{2}$$

The overall cell reaction is given by:

$$2Na + xS \leftrightarrow Na_2S_x \tag{3}$$

where x is the variable subscript for sulfur in the sodium-polysulfide melt. The forward reaction takes place during cell discharge when the positive sodium ions move from the anode to the cathode through the beta"-alumina electrolyte. The beta"-alumina electrolyte is practically impermeable to electrons [23,42]. Sodium ions react with the liquid sulfur in the cathode to produce sodium polysulfides. Under fully charged condition, the sulfur electrode contains only sulfur. As discharge operation begins, the sulfur electrode transitions to a two-phase mixture of sulfur and polysulfide. As the reaction progresses, more sodium ions react with the sulfur and the mole fraction of total sulfur decreases. Composition of the sulfur electrode changes based on the amount of sodium that crosses the electrolyte. The sodium polysulfide composition in the melt is denoted by the subscript 'x' in Reaction (3). The phase of the melt changes depending on the SOD of the cell since 'x' changes depending on the SOD. At a mole fraction of about 0.729, the sulfur electrode becomes single-phase polysulfide until the melt reaches 0.571 mol fraction sulfur [29]. At this point the solid polysulfide Na_2S_2 begins to form and proper operation of the cell is no longer possible. Therefore, the cell is considered to be fully discharged when the sulfur electrode composition reaches Na_2S_3.

It is desired that the anode and cathode materials stay in the liquid phase for proper operation of the cell. The sodium sulfur battery usually operates between 300 and 400 °C, at which temperature of the sodium, sulfur, and polysulfides (Na_2S_5–Na_2S_3) exist in the liquid phase [23]. The open circuit voltage of the cell at 350 °C is 2.075 V [23]. The specific energy density of the battery reaches 760 Wh/kg at 350 °C, nearly three times that of a lead acid battery [7].

The sodium electrode contains a stainless steel wick that is in direct

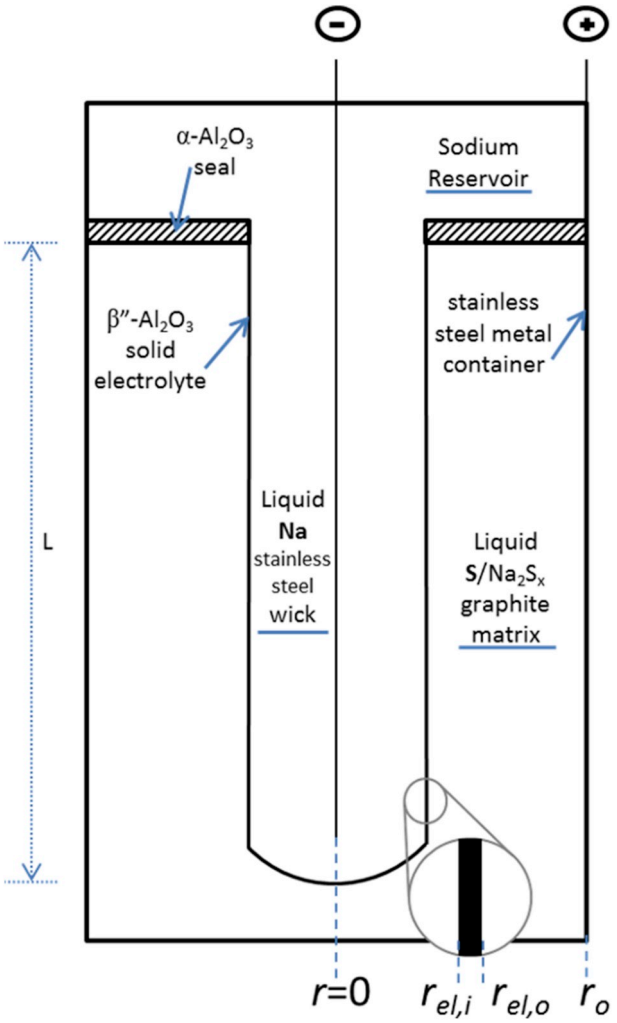


Fig. 1. Schematic of a central sodium sulfur cell.

contact with the inner side of the beta"-alumina electrolyte, allowing for complete wetting of the electrolyte surface with liquid sodium. The sulfur/sodium polysulfide melt is contained in a graphite matrix for better electron conduction in the sulfur electrode.

2.1. Model development

The following assumptions are made in developing the model:

- variation in the cell potential, temperature, and concentration gradients in the axial direction are negligible.
- Convective flux in the cell compartments are negligible.
- the supply of sodium to the sodium electrode is abundant over the entire range of operation assuming that a large reservoir for sodium is available.
- the sodium electrode/beta"-alumina electrolyte interface is always completely wetted.

2.1.1. Sulfur electrode

The energy conservation equation for the sulfur electrode is given by:

$$\rho_{(S)} c_{p(S)} \frac{\partial T_{(S)}}{\partial t} - \frac{1}{r}\frac{\partial}{\partial r}\left(r\lambda_{(S)}\frac{\partial T_{(S)}}{\partial r}\right) = q_{(S)} \tag{4}$$

where r ρ, c_p, λ, T, t, and q denote the radius, density, specific heat, thermal conductivity, temperature, time, and the heat source per unit volume for the sulfur electrode, respectively with the (S) subscript denoting sulfur electrode. Temperature-dependent correlation, equation (A1) as shown in the Appendix, has been developed for the thermal conductivity of sodium polysulfides and liquid sulfur using the data available in the open literature [22]. This correlation can be found in Table 1 and more information is provided under the Appendix. Density and specific heat of the sulfur electrode are assumed to be constant as reported in Table 1 [22]. Additional information is provided under the Appendix. The heat source term is given by:

$$q_{(S)} = Q_{Ohmic} + Q_{Entropy} \tag{5}$$

$$Q_{Ohmic} = \frac{1}{\sigma_{e(S)}}\left(\frac{I}{2\pi r L}\right)^2 \tag{6}$$

$$Q_{Entropy} = \frac{a_s}{K_p}(\phi_{e(S)} - \phi_{i(S)} - \mu)\left(T\frac{dE}{dT}\right) \tag{7}$$

Here, σ_e, a_s, K_p, ϕ_e, ϕ_i, μ, and dE/dT denote the electronic conductivity of the melt, surface area per unit volume of graphite matrix, the surface polarization resistance coefficient, electronic and ionic potential, local potential, and temperature dependence of open circuit voltage, respectively.

The term $(\phi_{e(S)} - \phi_{i(S)} - \mu)$ is called the overpotential, which changes sign depending on whether the cell charging or discharging. The values for electronic conductivity, surface area per unit volume, and polarization coefficient are obtained from the open literature [37]. The term(dE/dT), typically known as the entropy term, depends on the SOD [34]. The developed correlation between the entropy and SOD and its fit to the experimental data are shown in Equation (A2) and Figure A2, respectively, under the Appendix. The SOD is also a function of the melt composition as shown in Equation (A3).

The local potential is given by the following equation:

$$\mu = \begin{cases} 2.05, & M \geq 0.710286 \\ \alpha_1 + \beta_1 X_e, & M < 0.710286 \end{cases} \tag{8}$$

Here, α_1 and β_1 are overpotential coefficients [43], M is the mole fraction sulfur, and X_e is the mole fraction 'electrolyte' (Na_2S) in the sulfur electrode [44,45]. The overpotential coefficients are functions of temperature, given by equation (A4) and equation (A5) as shown in Table 1. Additional explanation is provided under the Appendix using Figure A3. The mole fraction of sulfur is related to the mole fraction of electrolyte by:

$$X_e = 1/X_S \tag{9}$$

$$M = X_S/(2 + X_S) \tag{10}$$

where X_S is the value of the subscript x in Na_2S_x. The sodium ion conservation equation in the sulfur electrode is given by Ref. [37]:

$$\frac{\partial C_{+(S)}}{\partial t} = -\frac{1}{F}\frac{a_s}{K_p}(\phi_{e(S)} - \phi_{i(S)} - \mu) \tag{11}$$

where C_+ and F are the concentration of sodium ions and Faraday's constant. Charge conservation in the sulfur electrode leads to Equations (12) and (13) [44]:

$$-\sigma_{i(S)}\frac{\partial}{\partial r}\left(r\frac{d\phi_{i(S)}}{dr}\right) + r\frac{a_s}{K_p}\phi_{i(S)} = \frac{1}{3}FD_{(S)}\left(\frac{3t_+ - 1}{t_+(1-t_+)}\right)\frac{\partial}{\partial r}\left(r\frac{dC_{+(S)}}{dr}\right) + r\frac{a_s}{K_p}(\phi_{e(S)} - \mu) \tag{12}$$

$$-\sigma_{e(S)}\frac{\partial}{\partial r}\left(r\frac{d\phi_{e(S)}}{dr}\right) + r\frac{a_s}{K_p}\phi_{e(S)} = r\frac{a_s}{K_p}\left(\phi_{i(S)} + \mu\right) \tag{13}$$

Here,σ_i, D, and t_+ are the ionic conductivity, diffusion coefficient of sodium ions, and the transference number of sodium ions in the sulfur

Table 1
Additional equations for sulfur electrode.

Variable Notation	Equation/Value	Units	Reference/Comments
$\lambda_{(S)}$	$0.4813 - 1.8648 \times 10^{-3} T_{(S)} + 2.4844 T_{(S)}^2$	W/mK	[22,48]
$\rho_{(S)}$	1880	kg/m^3	[22]
$c_{p(S)}$	1315	J/kgK	[22]
$\sigma_{e(S)}$	50	A/V	[37]
a_s	$a_{s0}(1 - p_{(S)}) \begin{cases} \times 1, & X_S < 5.24 \\ \times (5.24/X_S), & X_S > 5.24 \end{cases}$	m^2/m^3	[37]
$p_{(s)}$	0.35	–	[51]
a_{s0}	1×10^4	m^2/m^3	[37]
K_p	1×10^{-4}	Ω/m^2	[37]
$T\frac{dE}{dT}$	$-15.536(SOD)^5 + 32.652(SOD)^4 - 22.969(SOD)^3 + 6.0576(SOD)^2 - 0.5629(SOD) - 0.0362$	V	This work
α_1	$(-8.1667 \times 10^{-5})(T_{(S)}) + 2.5087$	V	[43]
β_1	$(-7.350 \times 10^{-4})(T_{(S)}) - 1.5600$	V	[43]
β_3	$(3.0783 \times 10^{-3})(T_{(S)}) + 0.0472$	V	[43]
X_s	$(2/C_+)(W_s/32)(1/V_{(S)})$	–	[44,45]
F	9.6487×10^7	C/kmol	Faraday's constant
t_+	$(-\beta_3/\beta_1 - X_e)/(1 - X_e)$	–	[43]
$\sigma_{i(S)}$	$\sigma_{i0(S)}(1 - p_{(S)})$	A/V	[44,45]
$\sigma_{i0(S)}$	$\begin{cases} -457.04M + 657.04, & M \geq 0.72 \\ -242.99M + 207.75, & 0.60 > M > 0.72 \\ 61.956, & M \leq 0.60 \end{cases}$	1/ohm.m	[44,45]
$D_{(S)}$	$(1.53 \times 10^{-6}) exp(-8590/T_{(S)}) exp(5.30 X_e)$	m^2/s	[46]
SOD	$\begin{cases} -343.55M + 304.82, & single\ phase\ polysulfide \\ -202.43M + 202.23, & two\ phase\ sulfur/polysulfide \end{cases}$	Ah(max)/Ah	This work
$V_{(S)}$	9.5425×10^{-5}	m^3	–
α	30	W/m^{2}K	[22]
ε	0.066	–	[36,52]
δ	5.67×10^{-8}	W/m^{2}K^4	Stefan-Boltzmann constant
W_s	0.1	kg	[37]

electrode, respectively. The ionic conductivity of the sodium polysulfide melt is a function of the mole fraction of sulfur in the melt [44,45] as shown in Table 1. The diffusion coefficient (Table 1) for sodium ions in the melt is a function of temperature and mole fraction of the electrolyte (Na_2S) in the melt [46]. The transference number (Table 1) of sodium ions is based on the overpotential coefficients β_1, β_3 and the mole fractional of electrolyte as shown in Table 1 and is based on the experimental cells of Risch and Newman [43].

2.1.2. Beta"-alumina electrolyte

The energy conservation equation in the beta"-alumina solid electrolyte is given by:

$$\frac{\partial T_{(el)}}{\partial t} = \frac{1}{\rho_{(el)} c_{p(el)} r} \left(q_{(el)} r + \frac{\partial}{\partial r} \left(r \lambda_{(el)} \frac{\partial T_{(el)}}{\partial r} \right) \right) \tag{14}$$

where ρ and c_p denote the density and specific heat capacity of the electrolyte respectively, with subscript denoting the beta-alumina electrolyte. The temperature-dependent correlation for density is determined based on the thermal expansion coefficient and is shown in Table 2. The density is given by equation (A7) in the Appendix, where additional information is provided. The thermal expansion coefficient is given by Sudworth and Tilley [22]. The specific heat capacity and thermal conductivity of the electrolyte are also functions of temperature [47] as shown in Table 2.

The heat source term $q_{(el)}$ (W/m^3) in the electrolyte is mainly due to Ohmic heat loss and is given by:

$$q_{(el)} = \frac{J^2}{\sigma_{i(el)}} \tag{15}$$

where J is the current density. Sodium ion conduction in beta"-alumina electrolyte is mainly due to the ionic conductance and ion migration. The sodium ion conservation in the electrolyte is given by:

Table 2
Additional equations for Beta"-Alumina electrolyte.

Variable Notation	Equation/Value	Units	Reference/Comments
$\lambda_{(el)}$	$2.451 + 2.456 \times 10^{-4}(T_{(el)}) - 6.178 \times 10^{-7}(T_{(el)})^2 + 4.275 \times 10^{-10}(T_{(el)})^3 - 6.993 \times 10^{-14}(T_{(el)})^4$	W/mK	[47]
$\rho_{(el)}$	$3220 \exp(-3\alpha_L(T_{(el)} - 25))$	kg/m^3	[22]
$c_{p,(el)}$	$0.7321 + 5.006 \times 10^{-4}(T_{(el)}) - 2.151 \times 10^{-7}(T_{(el)})^2$	J/kgK	[47]
$D_{(el)}$	$D_0 exp[-H/(RT_{(el)})]$	m^2/s	[49]
$p_{(el)}$	$(3220 - \rho_{(el)})/3220$	–	[22]
$\sigma_{i(el)}$	$(\sigma_{0(el)}/T_{(el)}) exp[-H/(RT_{(el)})]$	1/ohm.m	[49]
$\sigma_{0(el)}$	1.49×10^6	K/Ωm	[49,50]
H	5.497	kcal/mol	[49,50]
α_L	7.5×10^{-6}	K^{-1}	[22]
p_t	1.8×10^{-4}	V/K	[53]
D_0	3.98×10^{-8}	m^2/s	[49]
H	5.497	kcal/mol	[49,50]

$$\frac{\partial C_{+(el)}}{\partial t} = \frac{D_{(el)}}{p_{(el)}} \frac{1}{r} \frac{\partial}{\partial r} \left(r \frac{\partial C_{+(el)}}{\partial r} \right) \tag{16}$$

where p is the porosity of the beta"-alumina electrolyte. The correlation for porosity is proposed as shown in Table 2. The equation is based on the theoretical and calculated density of sodium beta"-alumina, and describes it as a function of temperature, as shown in Equation (A8). More details about the correlation can be found in the Appendix.

Conservation of positive ions in the electrolytes is written by considering ion transport by both diffusion and migration:

$$-\sigma_{i(el)} \frac{\partial \phi_{i(el)}}{\partial r} - F D_{(el)} \frac{\partial C_{+(el)}}{\partial r} = J \tag{17}$$

The ionic conductivity, σ_i, and diffusion coefficient, D, are functions of temperature, as shown in Table 2. More information about these variables can be found in the Appendix, where the equation for ionic conductivity is given by Equation (A9) and for diffusion coefficient is given by Equation (A10).

2.1.3. Sodium electrode

The energy conservation for the sodium electrode can be written as:

$$\left(m_{ss} c_{p,ss}\right) \frac{\partial T_{(Na)}}{\partial t} + \left(m_{Na} c_{p,Na}\right) \frac{\partial T_{(Na)}}{\partial t} = q_{(Na)} + \left(2\pi r_{el,i} L \lambda_{(el)}\right) \frac{\partial T_{(el)}}{\partial r}\bigg|_{r=r_{el,i}} \tag{18}$$

where m is the mass and c_p is the specific heat, with subscripts *ss* and *Na* denoting the stainless steel wick and the liquid sodium in the sodium electrode. Specific heats are functions of temperature as shown in Table 3. They are given by Equations A11 and A12, respectively, in the Appendix, and explained in Figure A4. The heat source term, $q_{(Na)}$, for the sodium electrode considers the Ohmic heat loss at the interface of the electrolyte,

$$q_{(Na)} = \frac{I^2 \rho_{l(Na)} r_{el,i}}{2\pi (r_{el,i}/2) L} \tag{19}$$

where $\rho_{l(Na)}$ is the resistivity of liquid sodium. The resistivity of liquid sodium is a function of temperature [22], as shown in Table 3. The concentration of sodium ions at the beta"-alumina interface is given by:

$$\frac{\partial C_{+(Na)}}{\partial t} = \frac{-I}{F V_{(Na)}} \tag{20}$$

where V is the volume of the sodium electrode, including the molten sodium, the wick, and the reservoir. The ionic potential drop in the sodium electrode is given by:

$$\phi_{i(Na)} = -\eta_{(Na)} \tag{21}$$

where $\eta_{(Na)}$ is the linear current potential relationship shown in Table 3 is derived from Butler-Volmer kinetics. No electronic potential change is considered in the sodium electrode.

2.2. Boundary conditions

Table 4 lists the boundary conditions based on the following assumptions:

- The Peltier heat is released at the electrolyte-sulfur electrode interface.
- There is no loss of ions through the metal container boundary of the cell.
- Heat is lost to the surroundings from the outer wall of the metal container by both convective and radiative heat transfer mechanisms.

3. Results and discussion

The model is developed in Aspen Custom Modeler® V.8.4. and solved using method of lines.

3.1. Model validation

The model of the 80 Wh cell is validated at various current density operations and states of discharge/charge with the experimental data from the open literature [36,37]. Dimensions of the experimental cell are given in Table 5.

Fig. 2 show model validation for charging and discharging when the

Table 4
Boundary conditions.

Number	Location	Boundary Condition
Sodium Electrode (*Na*)/Beta"-Alumina Electrolyte (*el*):		
BC1	$r = r_{el,i}$	$C_{+(Na)} = C_{+(el)}$
BC2	$r = r_{el,i}$	$T_{(el)} = T_{(Na)}$
BC3	$r = r_{el,i}$	$\phi_{i(el)} = -\eta_{Na}$
Beta"-Alumina Electrolyte (*el*)/Sulfur Electrode (*S*):		
BC4	$r = r_{el,o}$	$C_{+(el)} = C_{+(S)}$
BC5	$r = r_{el,o}$	$T_{(el)} = T_{(S)}$
BC6	$r = r_{el,o}$	$-\lambda_{(el)} 2\pi r_{el,o} L \frac{\partial T_{(el)}}{\partial r} = -\lambda_{(S)} 2\pi r_{el,o} L \frac{\partial T_{(S)}}{\partial r} \pm I p_t T_{(S)}$
BC7	$r = r_{el,o}$	$-\sigma_{i(el)} \frac{\partial \phi_{i(el)}}{\partial r} - F D_{(el)} \frac{\partial C_{+(el)}}{\partial r} = J$
BC8	$r = r_{el,o}$	$-\sigma_{i(S)} \frac{\partial \phi_{i(S)}}{\partial r} - F D_{(S)} \frac{\partial C_{+(S)}}{\partial r} = J$
BC9	$r = r_{el,o}$	$\phi_{i(el)} = \phi_{i(S)}$
BC10	$r = r_{el,o}$	$\frac{\partial \phi_{e(S)}}{\partial r} = 0$
Sulfur Electrode (*S*)/Metal Container:		
BC11	$r = r_o$	$\frac{\partial C_{+(S)}}{\partial r} = 0$
BC12	$r = r_o$	$\frac{\partial T_{(s)}}{\partial r} + \left(\frac{\alpha}{\lambda_{(S)}}\right)\left(T_{(S)} - T_{air}\right) + \left(\frac{\varepsilon\delta}{\lambda_{(S)}}\right)\left(T_{(S)}^4 - T_{air}^4\right) = 0$
BC13	$r = r_o$	$\frac{\partial \phi_{i(S)}}{\partial r} = 0$
BC14	$r = r_o$	$\phi_{e(S)} = \phi_0$ so as to satisfy: $I = -2\pi L \int_{r_{el,o}}^{r_o} \left(\frac{a_s}{K_p}\right)\left(\phi_{e(S)} - \phi_{i(S)} - \mu\right) r dr$

Table 3
Additional equations for sodium electrode.

Variable Notation	Equation/Value	Units	Reference/Comments
m_{Na}	0.057	kg	[37]
m_{ss}	20.3	kg	[22], linearly scaled to cell dimensions
$c_{p,ss}$	$-4.591 \times 10^{-4}(T_{(Na)})^2 + 0.4813(T_{(Na)}) + 444.99$	J/kgK	[22]
$c_{p,Na}$	$1437.08 - 0.58063(T_{(Na)}) + 4.624 \times 10^{-4}(T_{(Na)})^2$	J/kgK	[22]
$\rho_{l(Na)}$	$6.87 \times 10^{-8} + 2.44 \times 10^{-10} T_{(Na)} + 2.67 \times 10^{-13}(T_{(Na)})^2 + 1.07 \times 10^{-15}(T_{(Na)})^3 - 2.67 \times 10^{-18}(T_{(Na)})^4$	Ohm.m	[22]
$V_{(Na)}$	2×10^{-3}	m^3	[37]
$\eta_{(Na)}$	$(IRT_{(Na)})/(2\pi r_{el,i} L i_0 F)$	W/m^3	This work
i_0	5×10^4	A/m^2	[54]

total amount of the current from/to the cell is 3 A, 6 A, and 9 A, corresponding to the current density of 35.4 mA/cm^2, 70 mA/cm^2 and 106 mA/cm^2, respectively.

The results from the model for both charging and discharging compare well with the experimental data as shown in Fig. 2. During charging, the root-mean-square error (RMSE) for voltage is ~0.055 V, ~0.066 V, and ~0.041 V, at 3 A, 6 A, and 9 A, respectively. During discharging, the RMSE is ~0.0136 V, ~0.0356 V and ~0.0293 V at 3 A, 6 A, and 9 A, respectively. During discharging, the cell voltage is nearly constant when the operation is in the two-phase region (<55% SOD), and then decreases as the SOD increases further. During charging, the cell begins in the single-phase region at the sulfur electrode and the voltage continues to increase and becomes nearly constant once the melt is in the two-phase region. Similar to the observations of Kawamoto [37], inflections are found to occur at lower SOD. As the current density increases, there is a relative increase in the SOD at which the inflection occurs. The main reason for this is the steep concentration gradient near the sulfur electrode-electrolyte interface at lower SOD as shown in Fig. 4.

Kawamoto and Kusakabe [36] have reported experimental data of the voltage and cell outer surface temperature profiles for high current density operation. Kawamoto and Kusakabe [36] have also shown comparison of their model results with those experimental data. Fig. 3 shows the comparison between results from the model developed in this work, results from the model developed by Kawamoto and Kusakabe [36] and the experimental data [36] for cell voltage and temperature at the surface. There were no experimental data available for the temperature of the cell center so only results from both the models are compared. The experimental data correspond to an ambient temperature of 335 °C and the current density of 260 mA/cm^2 during charging and 390 mA/cm^2 during discharging. Root mean square error (RMSE) between the model developed here and the experimental data [36] as well as the model developed by Kawamoto and Kusakabe [36] and the experimental data [36] is shown in Table 6. It is observed from Fig. 3 and Table 6 that results from both models for the voltage profile compare well with the experimental data during charge. However, during discharging the results from this model for the voltage profile is considerably closer to the experimental data than that of Kawamoto and Kusakabe [36]. RMSE values from both models for the temperature profile is similar during charging, but the results for the temperature profile during discharging compare better with the experimental data than that of Kawamoto and Kusakabe [36]. The study also shows that even though the ambient temperature is held constant at 335 °C, the high current density operation leads to a temperature that is very close to the maximum temperature limit of 400 °C typically considered to be safe for sodium-sulfur cells. Since temperature of the cell at the center may be difficult to be measured in real life, a non-isothermal model can be very useful to avoid unsafe operation of the cell. To this end, one operational strategy can be to vary the current density of a given cell to maintain the cell temperature within the limit. This strategy is discussed in details in Section 3.4.3.

Table 5
Cell dimensions.

Parameter	Value	Units
L	0.18	m
$r_{el,i}$	0.0069375	m
$r_{el,o}$	0.0075	m
r_o	0.015	m
T_{air}	330	°C
$V_{(Na)}$	2×10^{-3}	m^3
$V_{(S)}$	9.5425×10^{-5}	m^3

3.2. Concentration distribution

As mentioned, when the cell discharges, the concentration of sodium ions in the beta"-alumina electrolyte and sulfur electrode increases, moving from the two-phase region (S, Na_2S_x) to the single-phase region (Na_2S_x). The electric conduction characteristics differ between these two regions. The overpotential term in Equation (11) alters sign as the cell switches from charging to discharging, which results in an overall increase in the sodium ion concentration during charging while a decrease during discharging as seen in Fig. 4. In addition, at the electrolyte/sulfur electrode interface, as SOD increases the Na ion concentration increases.

In the single phase region, diffusion due to the concentration gradient is negligible i.e., the electric conduction is dominated by migration. As stated in Section 2, the sulfur electrode becomes single phase when the sulfur mole fraction becomes about 0.729 and remains as a single phase until the sulfur mole fraction reaches 0.571. It can be observed form Equation (8) that in this region the local potential increases during charging due to the increase in overpotential coefficients that depend on the temperature. This affects the overpotential, which leads to an increase in the concentration gradient of sodium ions in the single phase region during charging. As seen in Fig. 4, when the SOD decreases, sodium ion concentration at the cathode becomes much smaller than at the anode thus the driving force term in the diffusive flux (Equation (12)) changes sign. Thus at the lower SOD, transport of sodium ions from the cathode to the anode needs an increasingly higher potential for overcoming the opposing concentration gradient that keeps rising. This leads to the steep rise in the voltage at lower SOD while charging. However, in the two-phase region the local potential is constant (Equation (8)), which results in nearly constant cell voltage. The voltage characteristics under discharging condition can be explained in a similar manner.

3.3. Temperature distribution

The temperature profiles within the cell at 60% SOD during discharging and charge is shown in Fig. 5. The ambient air temperature was maintained at 330 °C. The dotted line in the graph represent the electrolyte/sulfur electrode interface. As expected, higher current density operation results in higher temperatures within the cell. It can also be observed that there is a greater temperature increase during discharging than during charging. This is due to the electro-chemical reactions that take place in the sulfur electrode, which are exothermic during discharging and endothermic during charging. The temperature difference between the center of the cell and ambient conditions is nearly 3 times greater during discharging than charge. It should be noted that this creates a mismatch in heat generated during discharging and charge. Therefore, for maintaining the same cell temperature during charging and discharge, the heat removal rate should be different between charging and discharging even at the same SOD and same current density.

3.4. Impact of key operating conditions

Operating conditions can affect the dynamics of the NaS cell. First, the impact of different environment temperatures is evaluated. Second, the transient response of the cell at higher current density operation is studied. Dynamic responses of the cell under various load demands are also studied.

3.4.1. Impact of the cell Environment's temperature

For the experimental cell of Kawamoto and Kusakabe [36] and Kawamoto [37], the furnace air temperature was controlled. During real-life operation of large number of cells as in a battery, this ambient temperature is expected to vary depending on the thermal management strategy. Fig. 6 shows the cell voltage profile for different ambient temperatures.

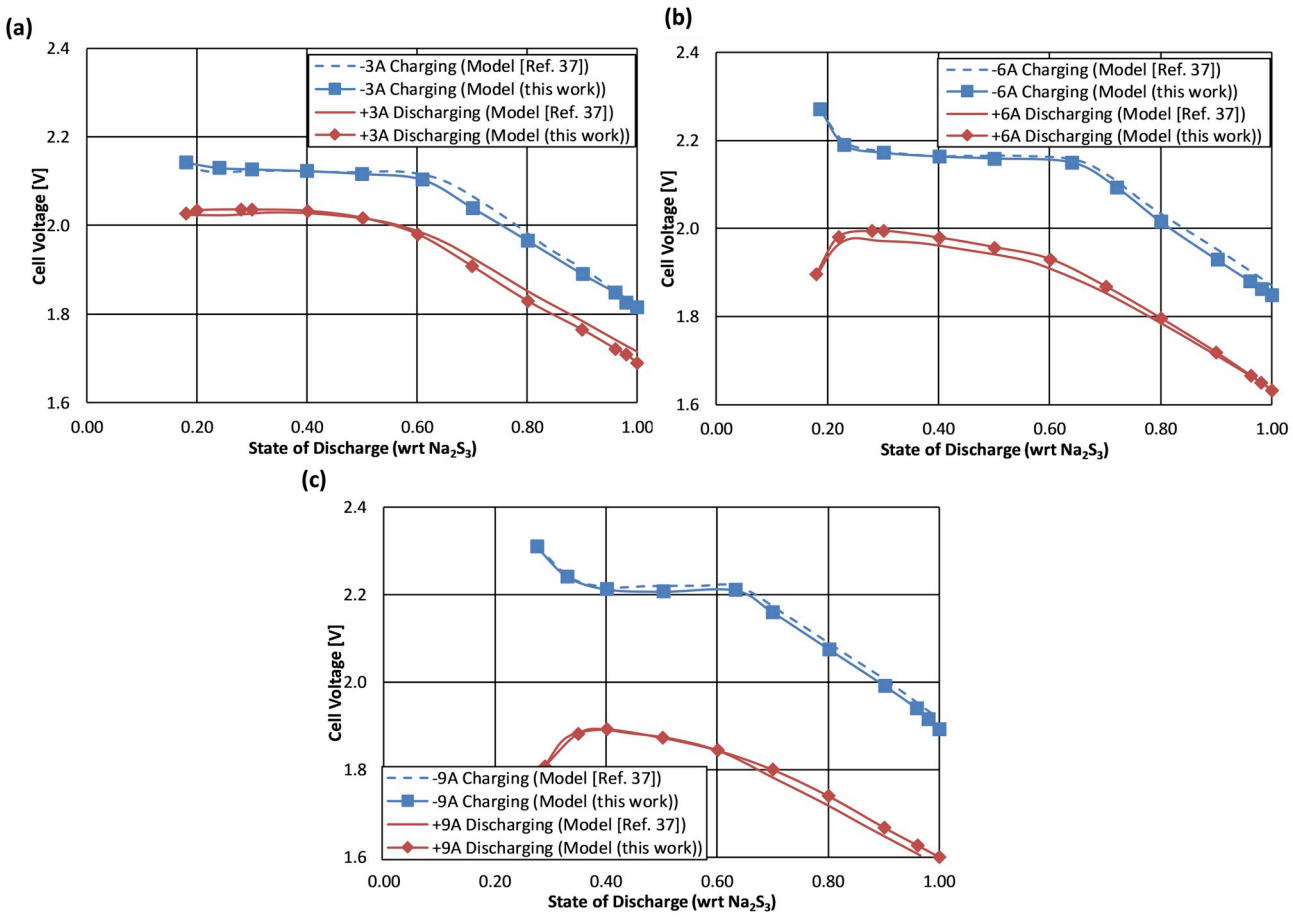


Fig. 2. Comparison between model results and experimental data from Kawamoto [37] for cell voltage vs SOD for an ambient temperature of 335 °C and during discharging/charge at (a) +/−3A corresponding to a current density of 35.4 mA/cm^2, (b) +/−6A corresponding to a current density of 70 mA/cm^2 and (c) +/−9A corresponding to a current density of 106 mA/cm.^{2}.

It is observed that the cell voltage profile is practically unaffected by the temperature under charging conditions whereas during discharging the cell voltage profile improves with the increase in the temperature. During charging as the cell approaches fully charged condition, the concentration of sulfur at the cathode/electrolyte interface keeps growing thus resulting in a higher cell resistance [31,37] or lower ionic conductivity. Since ionic resistance becomes the limiting mechanism during charging and the ionic conductivity is not affected directly by the cell temperature as can be observed in Table 1, an increase in the ambient temperature has negligible impact during charging. However during discharging, the limiting mechanism for a large range of SOD is the reaction overpotential and the reaction overpotential is strongly affected by the temperature as seen by Eq. (8) and the corresponding correlations for α_1 and β_1 in Table 1, the cell voltage profile improves during discharging as the ambient temperature is increased. Considering the entire discharge cycle shown in Fig. 6, the cell energy efficiency during discharging is about 91.92% at 330 °C compared to about 90.63% at 300 °C. It should be noted that while operation at higher temperatures can improve the cell efficiency, there is higher risk of fire hazard especially under high current density operation and rapid load changes as expected in grid-connected systems.

3.4.2. *Impact of high current density operation*

For a grid connected battery, high current density operation would be expected at certain time instants when the differences between demand and supply of electric power is very high. It is desired to study the impact of high current density operation on the cell temperature since increasing temperature can lead to a fire hazard. Fig. 7 shows the temperature profile within the cell at the end of discharge as the current density is changed while the ambient temperature is held constant at 335 °C. At high current density (390 mA/cm^2) operation, where the cell generates 33 A, the maximum cell temperature is about 38 °C higher in comparison to the maximum cell temperature when the current density is 70 mA/cm^2 generating 6A. The difference between the maximum and minimum temperature at 390 mA/cm^2 current density in the cell is almost 1.5 times that compared to the cell operating under a current density of 260 mA/cm^2 and almost 3 times more compared to a cell operating under a current density of 130 mA/cm^2 and almost 6 times more compared to a cell operating under a current density of 70 mA/cm^2. These results show that for safe operation of the cell under high current density operation, a model based approach can be valuable for monitoring and control since it is difficult to measure the temperature inside the cell in general.

3.4.3. *Impact of change in the current density*

Fig. 8 shows the transient response of cell voltage and temperature at the center and surface for high current density operation. It is observed that when higher current is drawn from the cell even at a similar OSD, the cell voltage decreases. The reverse happens during charging. Corresponding impact in the temperature profile can also be observed in Fig. 8. Note that the initial decrease in the temperature till about 0.5 h is due to the arbitrary initial temperature of the cell that is considered. As the current density is increased during charging at 0.5 h, the temperature at both locations starts increasing. As the current density is decreased at 1 h, both temperature starts decreasing. Similar behavior can be observed during discharging as well, i.e. temperature starts

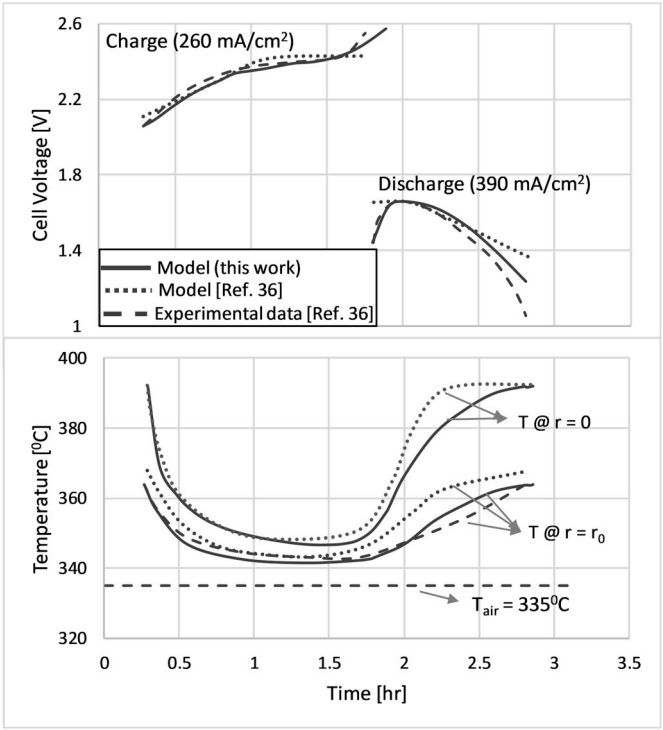


Fig. 3. Comparison between results from the model developed in this work, results from the model developed by Kawamoto and Kusakabe [36] and experimental data [36] for cell voltage and temperature at the surface and center (only model results compared as no experimental data available) of the cell at 335 °C ambient temperature and corresponding to the current density of 260 mA/cm^2 during charging and 390 mA/cm^2 during discharging.

increases as the current density is increased and vice versa. The behavior shows how the current density may be manipulated to ensure the cell remains within the safe operating limit. Since the highest temperature of the cell is at the center, a transient non-isothermal model can be useful to monitor that temperature and limit current density or regulate current density, if needed, to avoid unsafe operation.

4. Conclusions

A non-isothermal, transient model of the entire NaS cell with beta"-alumina electrolyte was modeled. The dynamic model was validated for various current density operations over SOD. The results from the model were found to agree well with the experimental data. It was observed that cell voltage profile can change considerably depending on the SOD, current density, temperature profile and whether the cell is charging or discharging. Inflection in the cell voltage profile was observed as the cell transitions from a single phase to a two-phase region. The inflection point is found to shift based on the current density. As the SOD decreases, sodium ion concentration at the cathode becomes much smaller than at the anode. Therefore, at the lower SOD, a higher potential is needed for transport of sodium ions from the cathode to anode to overcome the opposing concentration gradient. The higher cell temperature during discharging was observed because of the mismatch between the rates of heat generated during charging and discharging, due to the exothermic electrochemical reactions during discharging. It

Table 6
Root mean square error (RMSE) values between models and experimental data [36].

	Between Model developed in this work and the experimental data [36]	Model developed by Kawamoto and Kusakabe [36] and their experimental data [36]
Voltage (Charging)	~0.023 V	~0.036 V
Voltage (Discharging)	~0.078 V	~0.098 V
Temperature (Charging)	~2.1 °C	~2.5 °C
Temperature (Discharging)	~3.3 °C	~5.2 °C

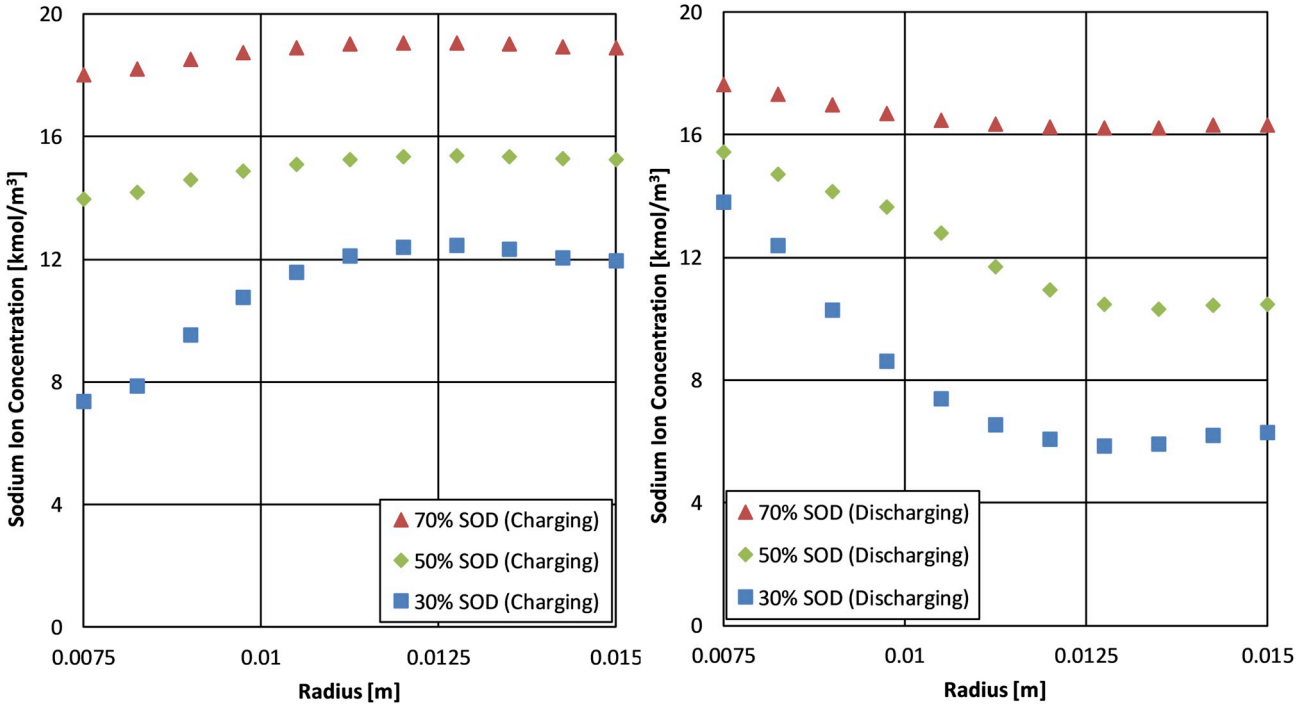


Fig. 4. Sodium ion concentration profile in the location between sodium/electrolyte interface to sulfur electrode during charging/discharge at ±6A at 70% SOD, 50% SOD and 30% SOD, respectively at 330 °C ambient temperature.

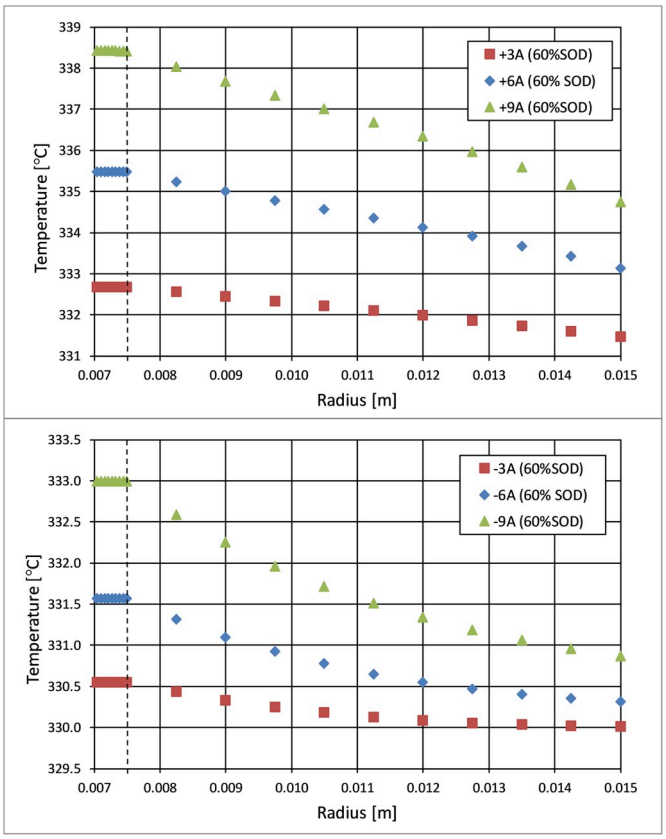


Fig. 5. Temperature profile in the cell during discharging and charge at 60% SOD for 3A, 6A and 9A current, respectively (corresponding to 35.4 mA/cm^2, 70 mA/cm^2 and 106 mA/cm^2 current density, respectively) for the ambient temperature of 330 °C (vertical dotted line represents the electrolyte/sulfur electrode interface).

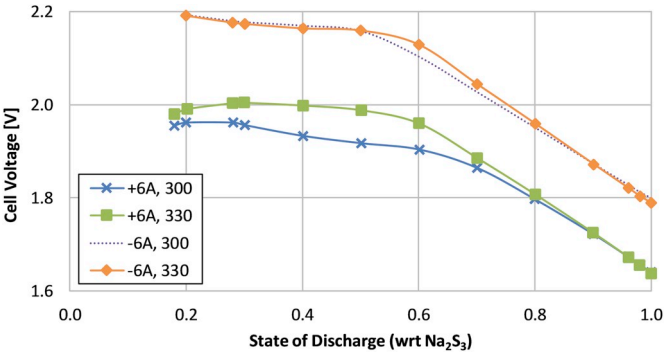


Fig. 6. Cell voltage vs SOD during discharging/charge at 300 °C and 330 °C ambient temperature for a current density of 70 mA/cm^2.

was observed that operating the cell at higher temperature can improve the cell efficiency. However higher temperature operation increases the risk of fire and therefore a proper thermal management strategy is desired. Changing the ambient temperature did have minor effect on the cell voltage during charging but improved the cell voltage profile during discharging. It was also observed that the current density can affect the cell voltage even at the same SOD. This aspect can be exploited for the battery power management.

It was observed that as the current density is increased, there is significant increase in the cell temperature. At the high current density operation considered in this study, the maximum temperature in the cell that occurs at the Na electrode is about 28 °C higher than the

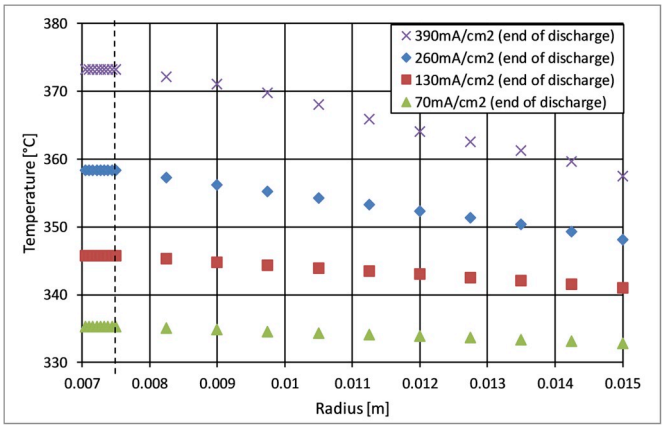


Fig. 7. Temperature profile in the cell at 70 mA/cm^2, 130 mA/cm^2, 260 mA/cm^2 and 390 mA/cm^2 current density, respectively, at 330 °C ambient temperature (vertical dotted line represents the electrolyte/sulfur electrode interface).

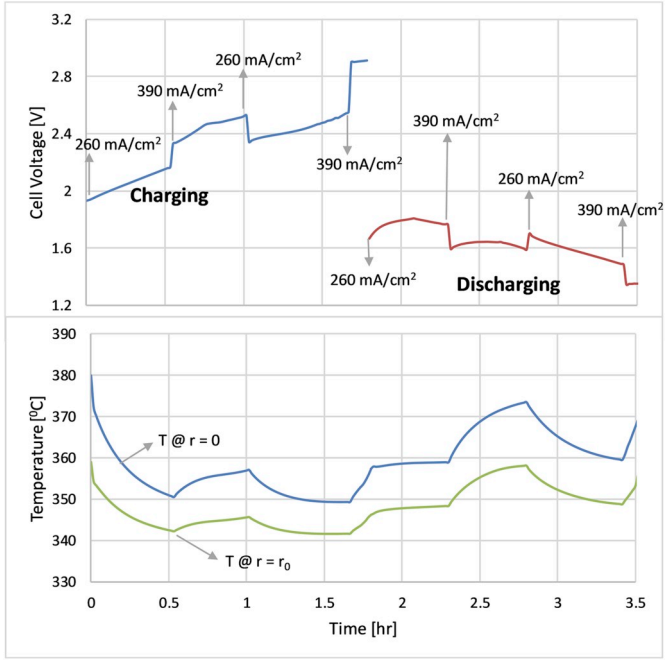


Fig. 8. Transient response of the cell voltage and temperature at the center and surface during discharging and charge for an ambient temperature of 335 °C.

environment temperature. Thus the study shows that if the cell environment temperature is maintained at a fixed value, it can lead to fire hazard for very high current density operation as would be expected for a grid-connected system. The study suggests two possible thermal management strategies: lowering the environment temperature, limit the current density to an upper limit depending on the environment temperature. However, as the cell produces very different amount of heat depending on whether it is charging or discharging and the current density, the thermal management approach must be able to remove variable amount of heat as well to maintain the cell temperature within a desired range.

The model presented here can be readily extended to room temperature NaS cells especially for studying the deviation in spatial and temporal temperature profile of those cells from the room temperature under charging/discharging conditions and how the deviation affects the cell efficiency and performance.

The model presented here can also be extended to Li–S cells. In Li–S

cells, the anode and the electrolytes are quite different than the Na–S cells. Even though there are certain differences between the cathodes of these two types of cells including the differences in the specific energy density, lowest state of sulfur that the cell can be discharged into, volumetric change during reaction, degradation mechanisms, to name a few, cathode reactions and electronic and ionic transport mechanisms are similar. Therefore, the model of the sulfur electrode presented here can be a very good starting point for modeling the cathode of the Li–S cells.

Declaration of competing interest

The authors declare that they have no known competing financial interests or personal relationships that could have appeared to influence the work reported in this paper.

Acknowledgement

The authors gratefully acknowledge the financial support from U.S. Department of Energy through U.S.-China Clean Energy Research Center (CERC) program under Cooperative Agreement DE-PI0000017.

Appendix A. Supplementary data

Supplementary data to this article can be found online at https://doi.org/10.1016/j.jpowsour.2020.227849.

Nomenclature

a_s	Surface area of graphite matrix per unit volume sulfur electrode (m^2/m^3)
a_{s0}	Net surface area of graphite matrix per unit volume sulfur electrode (m^2/m^3)
c_p	Specific heat capacity (J/kgK)
C_+	Concentration of sodium ions (kmol/m^3)
D	Diffusion coefficient (m^2/s)
D_0	Arrhenius constant for electrolyte diffusion coefficient (m^2/s)
dE/dT	Temperature dependence of open circuit voltage (V)
e-	Electron
F	Faraday constant (C/kmol)
H	Activation energy for sodium ion movement in electrolyte (kCal/mol)
I	Current (A)
i_0	Exchange current density of sodium electrode (A/m^2)
J	Current density ($C/s.m^2$)
K_p	Polarization coefficient ($ohm.m^2$)
L	Length of electrolyte (m)
M	Mole fraction elemental sulfur in sulfur electrode
m	Mass (kg)
MW	Molecular weight (kg/mol)
P	Porosity
p_t	Thermoelectric power (V/K)
q	Heat source term (W/m^3)
Q_{Ohmic}	Heat due to Ohmic losses (W/m^3)
$Q_{Entropy}$	Heat due to reaction (W/m^3)
R	Ideal gas constant (C/kmol K)
r	Radius (m)
$r_{el,i}$	Radius of inner electrolyte (m)
$r_{el,o}$	Radius of outer electrolyte (m)
r_o	Radius of outer cell container (m)
SOD	State of discharge (with respect to Na_2S_3) (Ah(max)/Ah)
T	Temperature (^0C)
T_{air}	Temperature of ambient air (^0C)
t	Time (s)
t_+	Transference number of sodium ions
V	Volume (m^3)
W_s	Weight of initially charged sulfur (kg)
x	Subscript in polysulfide, Na_2S_x
X_e	Mole fraction electrolyte (Na_2S)
X_s	Value of x in polysulfide, Na_2S_x

Greek Letters

α	Heat transfer coefficient between the cell container and the air (W/m^2K)
α_1	*Overpotential coefficient (Risch and Newman [43]) (V)*
α_L	Linear coefficient of thermal expansion for electrolyte (1/K)
β_1	*Overpotential coefficient (Risch and Newman [43]) (V)*
β_3	*Overpotential coefficient (Risch and Newman [43]) (V)*
δ	Stefan-Boltzmann constant (Wm^2/K^4)
ε	Effective emissivity
$\eta_{(Na)}$	Overpotential of sodium electrode (V)
λ	Thermal conductivity (W/mK)
μ	Local potential (V)
ρ	Density (kg/m^3)
$\rho_{l(Na)}$	Resistivity of liquid sodium (ohm.m)
σ_0	Arrhenius constant for electrolyte ionic conductivity (K/Ohm.m)
σ_e	Electronic conductivity (A/V)
σ_i	Ionic conductivity (A/V)
σ_{i0}	Net ionic conductivity of polysulfide melt (1/Ohm.m)
ϕ_0	Cell potential (voltage) (V)
ϕ_e	Electronic potential (V)
ϕ_i	Ionic potential (V)

Subscripts

air	Air in the furnace, surrounding sodium sulfur cell
(el)	Denotes variable within the beta"-alumina electrolyte
(Na)	Denotes variable within the beta sodium electrode
Na	Liquid sodium in the sodium electrode
(S)	Denotes variable within the beta sulfur electrode
ss	Stainless steel wick in the sodium electrode

References

[1] H. Ibrahim, A. Ilinca, J. Perron, Energy storage systems— characteristics and comparisons, Renew. Sustain. Energy Rev. 12 (2008) 1221–1250, https://doi.org/10.1016/j.rser.2007.01.023.

[2] P. Sarda, E. Hedrick, K. reynolds, D. Bhattacharyya, S.E. Zitney, B. Omell, Development of a Dynamic Model and Control System for Load-Following Studies of Supercritical Pulverized Coal Power Plants, vol. 6, 2018, p. 226, https://doi.org/10.3390/pr6110226.

[3] B. Sorensen, Renewable Energy Conversion, Transmission and Storage, first ed., AP, London, 2007.

[4] M. Beaudin, H. Zareipour, A. Schellenberglabe, W. Rosehart, Energy storage for mitigating the variability of renewable electricity sources: an updated review, Energy Sustainable Dev 14 (2010) 302–314, https://doi.org/10.1016/j.esd.2010.09.007.

[5] S. Nykamp, M.G. Bosman, A. Molderink, J.L. Hurink, G.J. Smit, Value of storage in distribution grids competition or cooperation of stakeholders smart grid, IEEE Trans 4 (3) (2013) 1361–1370, https://doi.org/10.1109/tsg.2013.2254730.

[6] D. Rastler, Electricity Energy Storage Technology Options: A White Paper Primer on Applications, Costs and Benefits, EPRI, Palo Alto, CA, 2010, 1020676, http://large.stanford.edu/courses/2012/ph240/doshay1/docs/EPRI.pdf.

[7] H. Mitavachan, D. Karen, V. Thomas, Comparitive life cycle assessment of battery storage systems for stationary applications, Environ. Sci. Technol. 49 (2015) 4825–4833, https://doi.org/10.1021/es504572q.

[8] B. Dunn, H. Kamath, J.M. Tarascon, Electrical energy storage for the grid: a battery of choices, Science 334 (6058) (2011) 928–935, https://doi.org/10.1126/science.1212741.

[9] B. Battke, T.S. Schmidt, D. Grosspietsch, V.H. Hoffmann, A review and probabilistic model of lifecycle costs of stationary batteries in multiple applications, Renew. Sustain. Energy Rev. 25 (2013) 240–250, https://doi.org/10.1016/j.rser.2013.04.023.

[10] R.S. Adam, F.R. Gregory, J.K. Robert, M.G. Brandon, T.S. Zachary, Survey of battery energy storage systems and modeling techniques, in: Proceedings of the 2012, IEEE Power and Energy Society General Meeting, San Diego, CA, USA, 22–26 July 2012, https://doi.org/10.1109/PESGM.2012.6345071, 1–8.

[11] D. Manz, J. Keller, Value propositions for utility-scale energy storage, in: Power Systems Conference and Exposition (PSCE), 2011, IEEE/PES, Phoenix, AZ, 2011, pp. 1–10, https://doi.org/10.1109/PSCE.2011.5772524.

[12] A.R. Dehghani-Sanij, E. Tharumalingam, M.B. Dusseault, R. Fraser, Study of energy storage systems and environmental challenges of batteries, Renew. Sustain. Energy Rev. 104 (2019) 192–208, https://doi.org/10.1016/j.rser.2019.01.023.
[13] K. Nestmeier, Grid-integrated storage systems, in: 6th International Renewable Energy Storage Conference and Exhibition, IRES 2011, Berlin, 2011, pp. 1188–1208.
[14] G. Girishkumar, B. McCloskey, A.C. Luntz, S. Swanson, W. Wilcke, Lithium-air battery: promise and challenges, J. Phys. Chem. Lett. 1 (2010) 2193–2203, https://doi.org/10.1021/jz1005384.
[15] A. Yoshino, Development of the Lithium-Ion Battery and Recent Technological Trends, Gianfranco Pistoia, Elsevier, 2014, pp. 1–20, https://doi.org/10.1016/B978-0-444-59513-3.00001-7.
[16] I. Kim, J.Y. Park, C.H. Kim, J.W. Park, J.P. Ahn, J.H. Ahn, K.W. Kim, H.J. Ahn, A room temperature Na/S battery using a β″ alumina solid electrolyte separator, tetraethylene glycol dimethyl ether electrolyte, and a S/C composite cathode, J. Power Sources 301 (2016) 332–337, https://doi.org/10.1016/j.jpowsour.2015.09.120.
[17] J.B. Goodenough, K.S. Park, The Li-ion rechargeable battery: a perspective, J. Am. Chem. Soc. 135 (2013) 1167–1176, https://doi.org/10.1021/ja3091438.
[18] G. Nikiforidis, M.C.M. van de Sanden, M.N. Tsampas, "High and intermediate temperature sodium–sulfur batteries for energy storage: development, challenges and perspectives, RSC Adv. 9 (2019) 5649–5673, https://doi.org/10.1039/C8RA08658C.
[19] C. Delmas, Sodium and sodium-ion batteries: 50 Years of research, Adv. Energy Mater. 8 (2018) 1703137 1–9, https://doi.org/10.1002/aenm.201703137.
[20] S. Wei, S. Xu, A. Agrawral, S. Choudhury, Y. Lu, Z. Tu, L. Ma, L.A. Archer, A stable room temperature sodium–sulfur battery, Nat. Commun. 7 (2016) 11722, https://doi.org/10.1038/ncomms11722.
[21] P. Adelhelm, P. Hartmann, C.L. Bender, M. Busche, C. Eufinger, J. Janek, Beilstein, "from lithium to sodium: cell chemistry of room temperature sodium-air and sodium-sulfur batteries", Journal of Nanotechnology 6 (2015) 1016–1055, https://doi.org/10.3762/bjnano.6.105.
[22] J. Sudworth, A. Tilley, The Sodium Sulfur Battery, Chapman and Hall, New York, 1985.
[23] T. Oshima, M. Kajita, A. Okuno, Development of sodium-sulfur batteries, Int. J. Appl. Ceram. Technol. 1 (3) (2004) 269–276, https://doi.org/10.1111/j.1744-7402.2004.tb00179.x.
[24] C.J. Rydh, B.A. Sandén, Energy analysis of batteries in photovoltaic systems. Part I: performance and energy requirements, Energy Convers. Manag. 46 (2005) 1957–1979, https://doi.org/10.1016/j.enconman.2004.10.003.
[25] D. Kumar, S. Kumar Rajouria, S.B. Kuhar, D.K. Kanchan, Progress and prospects of sodium-sulfur batteries: a review, Solid State Ionics 312 (2017) 8–16, https://doi.org/10.1016/j.ssi.2017.10.004.
[26] D. Kumar, Mohd Suleman, S.A. Hashmi, Studies on poly(vinylidene Fluoride-Co-Hexafluoropropylene) based gel electrolyte nanocomposite for sodium–sulfur batteries, Solid State Ionics 202 (2011) 45–53, https://doi.org/10.1016/j.ssi.2011.09.001.
[27] R. Carter, L. Oakes, A. Douglas, N. Muralidharan, A.P. Cohn, C.L. Pint, A sugar-derived room-temperature sodium sulfur battery with long term cycling stability, Nano Lett. 17 (2017) 1863–1869, https://doi.org/10.1021/acs.nanolett.6b05172.
[28] J. Kummer, N. Weber, US Patent 3 (1968) 413, 150.
[29] M. McKubre, F. Tanzella, S. Smedley, The electromotive force of the Na/S cell, J. Electrochem. Soc. 136 (2) (1989) 303–305, https://doi.org/10.1149/1.2096625.
[30] M. McKubre, S. Smedley, F. Tanzella, The electrochemical impedance of the Na/S cell I. Experiments and results, J. Electrochem. Soc. 136 (7) (1989) 1962–1968, https://doi.org/10.1149/1.2097101.
[31] J.G. Gibson, The distribution of potential and electrochemical reaction rate in molten polysulphide electrodes, J. Appl. Electrochem. 4 (1973) 125–134, https://doi.org/10.1007/BF00609021.
[32] M.W. Breiter, B. Dunn, Potential distribution model for rechargeable sulphur electrodes in sodium-sulfur cells, J. Appl. Electrochem. 9 (1979) 291–299, https://doi.org/10.1007/BF01112482.
[33] R. Knoedler, Calorimetric determination of the heat generation rate of sodium-sulfur cells during discharging and charge, J. Electrochem. Soc. 131 (4) (1984) 845–850, https://doi.org/10.1149/1.2115711.
[34] R. Knoedler, Thermal properties of sodium-sulfur cells, J. Appl. Electrochem. 14 (1984) 39–46, https://doi.org/10.1007/BF00611256.
[35] H. Kawamoto, Two-dimensional distribution of sodium polysulfide composition in sulfur electrodes of sodium-sulfur cells, J. Electrochem. Soc. 136 (7) (1989) 1851–1860, https://doi.org/10.1149/1.2097059.
[36] H. Kawamoto, Y. Kusakabe, Performance and thermal behavior of sodium-sulfur cell under high current density operations, J. Electrochem. Soc. 136 (5) (1989) 1355–1361, https://doi.org/10.1149/1.2096921.
[37] H. Kawamoto, Dynamic simulation of the charge-discharge characteristics of the sodium-sulphur cell, J. Appl. Electrochem. 21 (1991) 409–414, https://doi.org/10.1007/BF01024576.
[38] F.H. Zahrul, W.C. Lee, F.M.S. Mohd, B.I. Amir, Modeling of sodium sulfur battery for power system Applications, Elektrika 9 (2) (2007) 66–72.
[39] A.E. Sarasua, M.G. Molina, D.E. Pontoriero, P.E. Mercado, Modelling of NaS energy storage system for power system Applications, in: Transmission and Distribution Conference and Exposition: Latin America (T D-LA), IEEE/PES, 2010, pp. 555–560, https://doi.org/10.1109/TDC-LA.2010.5762937.
[40] J. Min, C. Lee, Numerical study on the thermal management system of a molten sodium-sulfur battery module, J. Power Sources 210 (2012) 101–109, https://doi.org/10.1016/j.jpowsour.2012.03.028.
[41] M. Aygun, A Computational Model for Thermal Management of Battery Storage Systems, Master's diss, West Virginia University, Morgantown, 2016. ProQuest (10195790).
[42] Z. Wen, J. Cao, Z. Gu, X. Xu, F. Zhang, Z. Lin, Research on sodium sulfur battery for energy storage, Solid State Ionics 179 (2008) 1697–1701, https://doi.org/10.1016/j.ssi.2008.01.070.
[43] T. Risch, J. Newman, Transference number calculations for sodium polysulfides, J. Electrochem. Soc. 135 (1988) 1715–1718, https://doi.org/10.1149/1.2096103.
[44] B. Cleaver, A. Davies, Properties of Fused polysulphides-III. EMF measurements on the sodium-sulphur cell, and sulphur activities and constitution in Fused sodium polysulphides, J. Appl. Electrochem. 18 (10) (1973) 733–739, https://doi.org/10.1016/0013-4686(73)80064-7.
[45] B. Cleaver, A. Davies, M. Hames, Properties of Fused polysulfides—I. The electrical conductivity of Fused Na and K polysulfides, Electrochim. Acta 18 (10) (1973) 719–726, https://doi.org/10.1016/0013-4686(73)80062-3.
[46] S.D. Thompson, J. Newman, Differential diffusion coefficients of sodium polysulfide melts, J. Electrochem. Soc. 136 (1989) 3362–3369, https://doi.org/10.1149/1.2096451.
[47] M.A. Ryan, R. Williams, C. Allevato, C. Vining, C. Lowe-Ma, S. Robie, Thermophysical properties of sodium β"-alumina polycrystalline ceramic, J. Phys. Chem. Solid. 55 (1994) 1255–1260, https://doi.org/10.1016/0022-3697(94)90207-0.
[48] G. Kaye, W. Higgins, Thermal conductivity of solid and liquid sulfur, in: Proceedings of the Royal Society, London, 1929, https://doi.org/10.1098/rspa.1929.0049.
[49] M. Whittingham, R. Huggins, Measurement of sodium ion transport in beta alumina using reversible solid electrodes, J. Chem. Phys. 54 (1971) 414–416, https://doi.org/10.1063/1.1674623.
[50] A. Virkar, G. Miller, R. Gordon, Resistivity-microstructure relations in lithia-stabilized polycrystalline β"-alumina, J. Am. Ceram. Soc. 61 (1978) 250–252, https://doi.org/10.1111/j.1151-2916.1978.tb09292.x.
[51] H. Kawamoto, M. Wada, Two-dimensional distribution of electrochemical reaction rate in porous sulfur electrodes of sodium-sulfur cells, J. Electrochem. Soc. 134 (1987) 280–285, https://doi.org/10.1149/1.2100446.
[52] H. Kawamoto, Numerical analysis on potential distribution and resistance of sodium-sulphur batteries, Denki Kagaku 52 (1984) 589–595.
[53] Y. Ito, N. Hayafuji, S. Yoshizawa, Energy Flow through beta-alumina solid electrolyte, Electrochim. Acta 30 (1985) 701–703, https://doi.org/10.1016/0013-4686(85)80114-6.
[54] A. Buechele, L. De Jonghe, D. Hitchcock, Degradation of sodium beta''-alumina - effect of microstructure, J. Electrochem. Soc. 130 (1983) 1042–1049, https://doi.org/10.1149/1.2119881.